Nanoscale

PAPER

View Article Online
View Journal

Check for updates

Cite this: DOI: 10.1039/d0nr00812e

Transparent photoactuators based on localized-surface-plasmon-resonant semiconductor nanocrystals: a platform for camouflage soft robots†

Feng Huang,[a,c,d] Mingcen Weng,[a,c,d] Zhuohong Feng,[a,c,d] Xiao Li,[b] Wei Zhang *[a,c,d] and Luzhuo Chen *[a,c,d]

Among the various kinds of actuators, photoactuators with the advantages of wireless and remote manipulation have attracted the interest of many researchers. However, it is challenging to develop transparent photoactuators for camouflage soft robots, because most of the current photoactuators use colored or even black light-absorbing agents. Here, we fabricate a series of transparent actuators by employing localized-surface-plasmon-resonant semiconductor nanocrystals, which mainly respond to infrared light. In this way, we introduce the advantages of wireless and remote manipulation into the camouflage soft robots. Three semiconductor nanocrystals (In_2O_3:Sn, $W_{18}O_{49}$ and CuS nanocrystals) are fabricated as the photothermal conversion agents to construct the photoactuators. Owing to the weak absorption of visible light, the fabricated actuators exhibit high transparency (maximum transmittance >72% at 600 nm). Meanwhile, they demonstrate remarkable deformations upon near infrared light irradiation (bending curvature up to 0.66 cm^{-1}). Finally, a worm-like crawling robot, a glasswing butterfly robot and a two-finger robot hand are constructed to demonstrate the ability of remote manipulation and inconspicuousness in both the robot appearance and the driving signal, attaining excellent passive camouflage function. These results provide a promising platform for remote-controlled camouflage soft robots and biomimic applications, which will be of significance in the field of soft robotics.

Received 30th January 2020,
Accepted 31st March 2020

DOI: 10.1039/d0nr00812e

rsc.li/nanoscale

Introduction

In the natural world, a transparent body is a facile and an effective camouflage strategy for animals. For example, *Greta oto* (glasswing butterfly) has transparent wings, so it can be naturally integrated into the background, reducing the risk of being discovered by eyesight-based predators.[1] Unlike the "initiative" camouflage strategy which needs prior information of the background and then matches with it, such so-called "passive" camouflage strategy is more facile. Animals can use this strategy for disguising themselves in their surrounding enviroments.[2] In view of this, developing transparent actuators would be of significance for the applications in camouflaging or namely "invisible" soft robots.

Up to now, several transparent actuators for camouflage soft robots have been developed. For example, Zhao *et al.* developed a hydraulic hydrogel actuator which could achieve complete immerging into the background, but needed to be immersed under water.[3] Tolley *et al.* developed translucent soft robots, which were driven by dielectric elastomer actuators, but were still operated in water.[4] Some other previous works were devoted to making transparent actuators operable in air. For example, thin graphene layers were used to construct actuators with appreciable transparency.[5–7] Super-aligned carbon nanotubes were employed as the electrical heating interlayer to construct electrothermal actuators with a transparent appearance.[8] In addition, silver nanowires were also applied as the electrical heating agent in transparent actuators.[9] However, these transparent actuators only responded to electrical stimulation, which made it difficult to

[a]Fujian Provincial Key Laboratory of Quantum Manipulation and New Energy Materials, College of Physics and Energy, Fujian Normal University, Fuzhou, 350117, China. E-mail: chenluzhuo@163.com, wzhang721@163.com
[b]Key Laboratory of Design and Assembly of Functional Nanostructures, Fujian Institute of Research on the Structure of Matter, Chinese Academy of Sciences, University of Chinese Academy of Sciences, Fuzhou, 350002, China
[c]Fujian Provincial Collaborative Innovation Center for Advanced High-Field Superconducting Materials and Engineering, Fuzhou, 350117, China
[d]Fujian Provincial Engineering Technology Research Center of Solar Energy Conversion and Energy Storage, Fuzhou, 350117, China

†Electronic supplementary information (ESI) available. See DOI: 10.1039/d0nr00812e

realize wireless manipulation. Hence, they were dissatisfactory for achieving a true sense of "invisibility" or "camouflage" since non-transparent wires were connected on the actuators.

Photoactuators are a good option with the advantages of operability in air and wireless and remote manipulation. However, it is challenging to make the photoactuators transparent and non-colored, since they always include colored or even black light-absorbing agents (such as dyes, pigments, toners, noble metal nanoparticles or carbon-based materials).[10–12] Searching for new light-absorbing agents, which are transparent in visible light range and which can absorb non-visible light, is a possible solution to this dilemma. Infrared absorbing dye was reported to be a candidate and applied by Zhao *et al.*[13] However, considering that the photochemical activities of dyes would exhibit the hidden peril of being bleached, it would be a better choice to utilize inorganic nanomaterials.

Herein, we develop a series of photoactuators with high transparency, introducing the advantages of remote-type stimulation and wireless manipulation into the camouflage soft robots. We employ semiconductor nanocrystals (SNCs) with localized-surface-plasmon-resonant (LSPR) behavior,[14–20] including In_2O_3:Sn (ITO) nanoparticles, $W_{18}O_{49}$ nanorods and CuS nanoplates, as the photothermal conversion agents. Polyethylene terephthalate (PET) and biaxially oriented polypropylene (BOPP) are selected as the polymer layers with different thermal expansion behaviors, forming the multilayer actuator structure. It is found that the SNC-based actuators exhibit high transmittance for visible light (maximum transmittance is in the range of 72%–82%), and can achieve remarkable deformation (maximum bending curvature up to 0.66 cm^{-1}) upon near infrared (NIR) light irradiation (500 mW cm^{-2}). A worm-like crawling robot, a glasswing butterfly robot and a two-finger robot hand are fabricated to demonstrate the advantages of such transparent actuators with remote and invisible manipulation as well as the feasibility of passive camouflage strategy. These results show the ability of remote manipulation and inconspicuousness in both the actuator appearance as well as the driving signal. This study would provide significant inspirations for the development of camouflage soft robots and biomimic applications.

Results and discussion

Fabrication and characterization

In the past decade, several SNCs, such as ITO, WO_x, CuS, Cu_2Se, $Cu_{1.94}S$ nanocrystals, *etc.*, have been reported to present the LSPR behavior, namely LSPR-SNCs.[14–20] Such a feature endows these nanomaterials with strong extinction cross-section to the photons with a specific wavelength. Unlike the conventional noble metal nanoparticles, whose LSPR light-extinction peaks always locate in the visible region, SNCs usually exhibit a resonant peak at the infrared region. What's more, owing to the existence of semiconductor band gaps, there are always "transparent windows" between the inter-band absorption edge and the LSPR extinction band. Such "transparent windows" can cover most of the visible light region and be favorable for fabricating transparent devices. Last but not least, unlike the noble nanoparticles, whose LSPR light-extinction property is composed of parallel scattering and absorption effect, the light extinction of LSPR-SNCs is mainly composed of absorption effect, owing to the large dielectric dissipation factor of the semiconductors.[21] It means that the LSPR-SNCs have a higher photothermal conversion ability than that of the noble nanoparticles. All these features imply the potential eligibility of the LSPR-SNCs for acting as the active component in transparent photothermal actuators.

In this work, we synthesized three kinds of LSPR-SNCs, including ITO nanoparticles, $W_{18}O_{49}$ nanorods and CuS nanoplates, and introduced them as the photothermal conversion agents. It is a pioneering experimental demonstration for the propitiousness of LSPR-SNCs in transparent photothermal actuators.

The LSPR-SNCs were fabricated through a thermolysis method and made into oily inks for constructing the photothermal conversion interlayer of transparent actuators (see Experimental section for details). The transmission electron microscopy (TEM) images of the prepared LSPR-SNCs are shown in Fig. 1A–C. As it can be observed, all the three kinds of nanocrystals are well dispersed. X-ray diffraction (XRD) patterns shown in Fig. S1 (ESI†) reveal that these products are indexed to ITO, $W_{18}O_{49}$ and CuS, respectively, without any detectable impurity diffraction peak. The ITO products exhibit uniform particle-like morphology with the size of ~10 nm. The $W_{18}O_{49}$ products are ~3 nm wide and ~15 nm long nanorods, while the CuS products are hexagonal nanosheets. The high-resolution TEM (HRTEM) images (Fig. S2, ESI†) show that each individual nanocrystal is monocrystalline. The appearances of colloidal oily inks made of these three kinds of LSPR-SNCs are clear and translucent, as shown in Fig. 1D. The observable color is ascribed to the concentration of nanocrystals in these inks. Fig. 1E shows the absorption spectra of the three kinds of inks. Obviously, all the inks exhibit a LSPR extinction band in the NIR region. The extinction peak of ITO ink locates at 1930 nm, while the peak of $W_{18}O_{49}$ ink locates at 2100 nm, and that of CuS ink is at 1180 nm. At the short-wave side (near the UV range), there are absorption edges corresponding to the interband transitions of these three semiconductors. As expected, in the spectral range between the absorption edges and the LSPR extinction bands, there are weak extinction regions for these three inks, which just coincide with the visible spectral range, indicating good transparency of these inks.

It is worth noting that, for these LSPR semiconductor nanocrystals, the wavelengths of plasmonic resonant peaks are all much larger than the particle sizes. According to the electrostatic approximation theory, in such case, the resonant extinction would be dominated by absorption behaviors, indicating superior photothermal conversion ability. To confirm this, we performed finite-difference-time-domain (FDTD) simulations to estimate the absorption and scattering cross-sections of

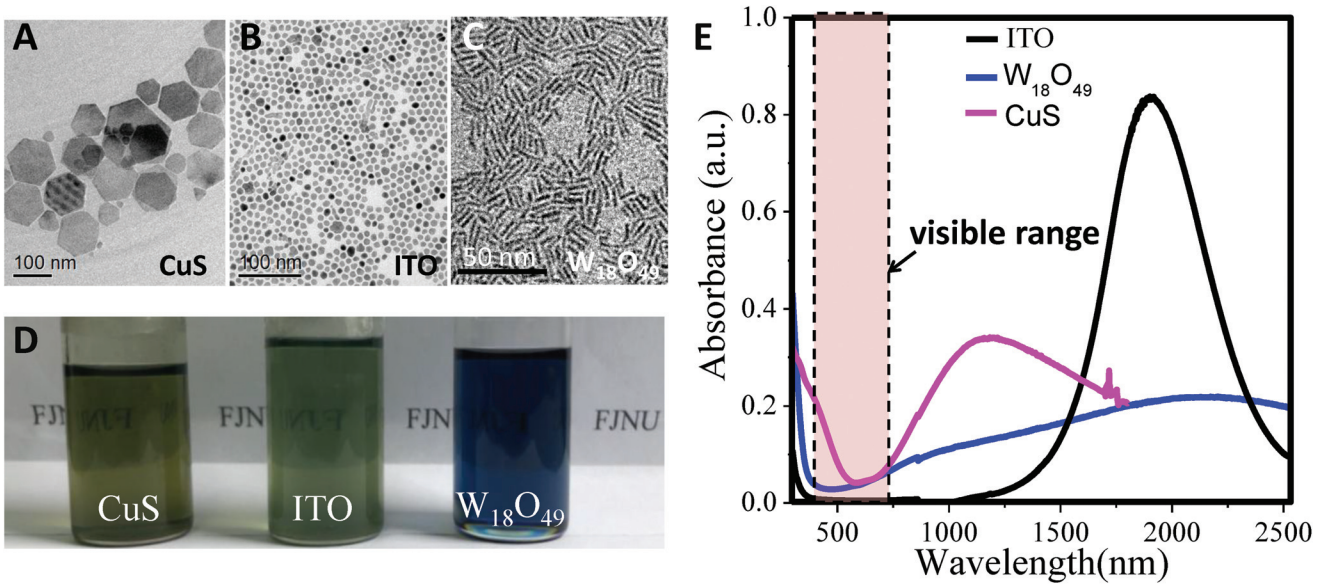

Fig. 1 TEM images of the synthesized nanocrystals. (A) CuS nanoplates. (B) ITO nanoparticles. (C) $W_{18}O_{49}$ nanorods. (D) Photographs of the CuS-, ITO- and $W_{18}O_{49}$-based inks. (E) Absorption spectra of the prepared oily inks containing ITO, $W_{18}O_{49}$ and CuS nanocrystals.

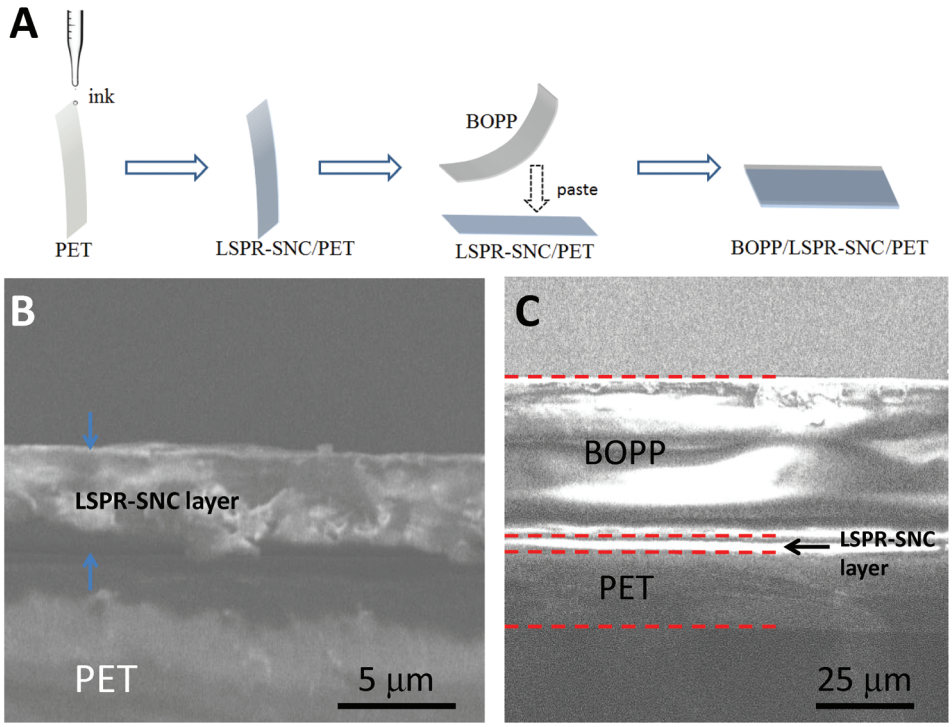

Fig. 2 (A) Schematic illustration demonstrating the fabrication process of BOPP/LSPR-SNC/PET actuators. (B) Cross-sectional SEM image of the ITO/PET bilayer film. (C) Cross-sectional SEM image of the BOPP/ITO/PET actuator.

these LSPR-SNCs. The simulation details are shown in Note S1 and Fig. S3 of the ESI.† The results exhibit that the absorption cross-sections for these LSPR-SNCs are all much larger than the scattering cross-sections (Fig. S4, ESI†), which implies a favorable photothermal conversion ability.

Fig. 2A shows the fabrication process of the actuators. Firstly, the prepared LSPR-SNC inks were coated on 25 μm-thick PET substrates by drop-casting. Owing to the compatibility between PET and the solvent of the LSPR-SNC inks (toluene), the LSPR-SNC inks could spread out easily, forming

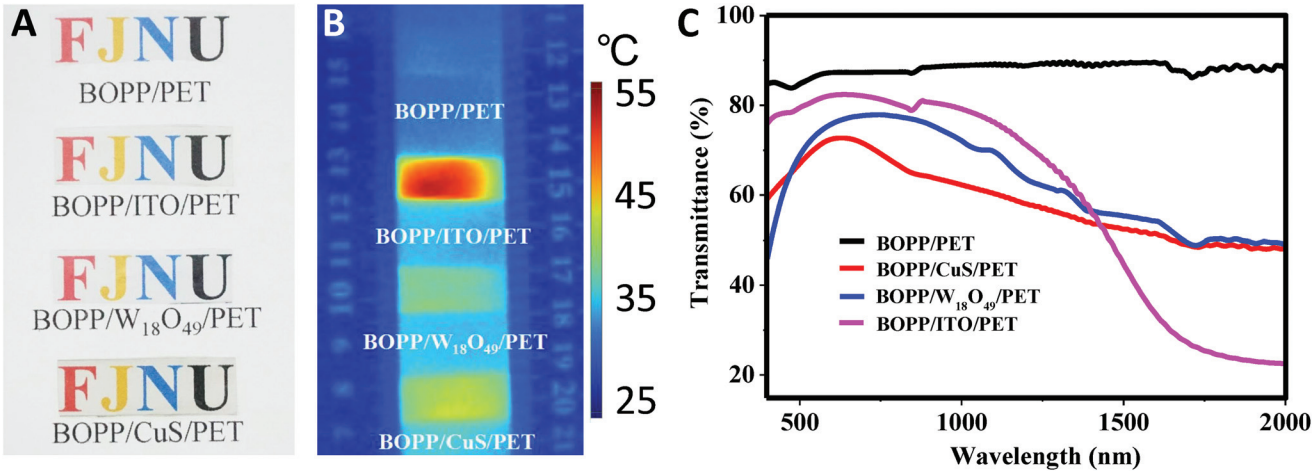

Fig. 3 (A) Photographs of the BOPP/LSPR-SNC/PET actuators and the BOPP/PET film. (B) Infrared thermal image of the BOPP/LSPR-SNC/PET actuators and the BOPP/PET film under NIR light irradiation (200 mW cm^{-2}). (C) Transmittance spectra of the BOPP/LSPR-SNC/PET actuators and the BOPP/PET film.

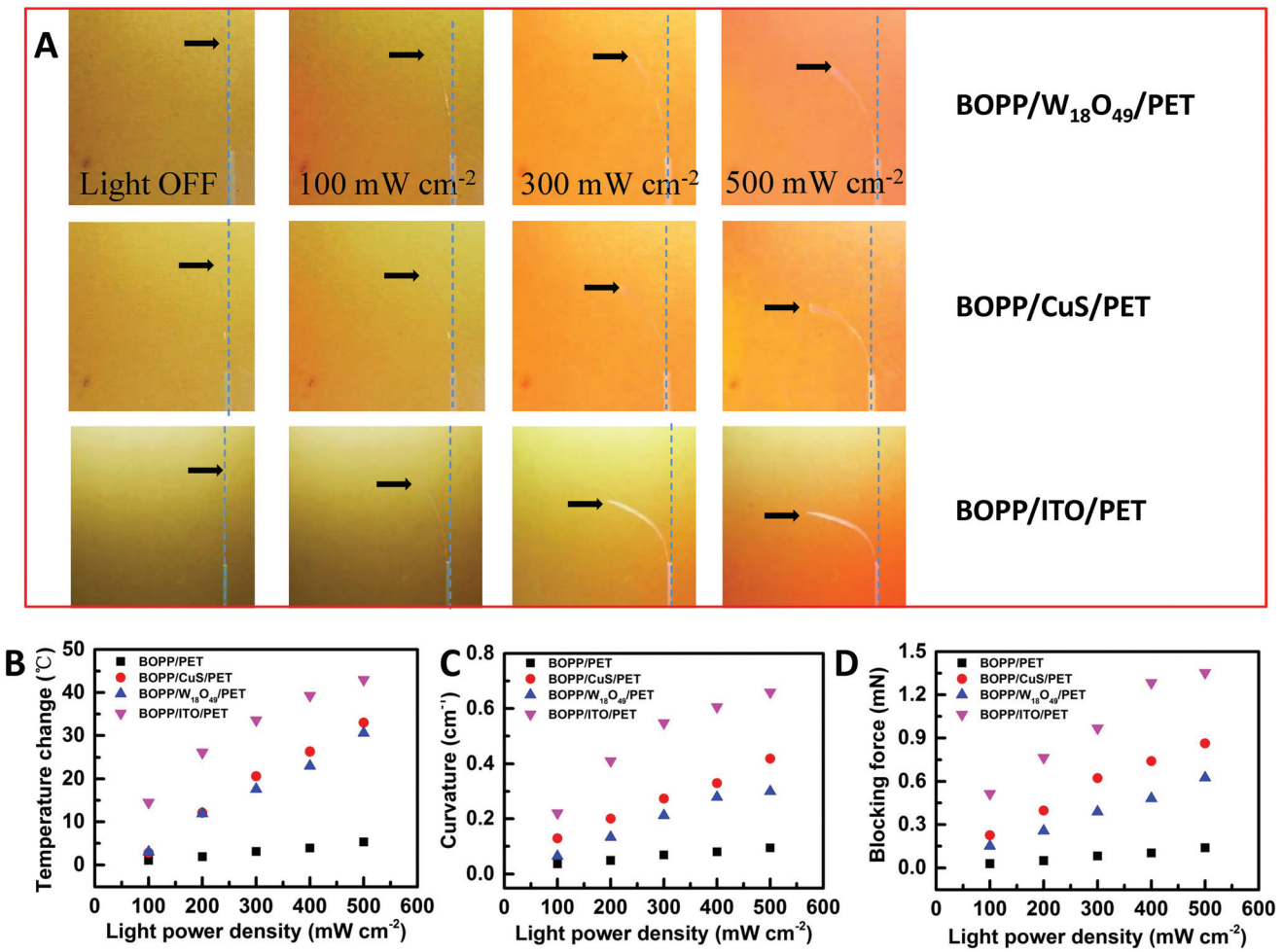

Fig. 4 (A) Photographs displaying the deformations of the BOPP/LSPR-SNC/PET actuators upon NIR light irradiation (0 to 500 mW cm^{-2}). (B) Temperature change as a function of light power density, corresponding to the BOPP/LSPR-SNC/PET actuators and the BOPP/PET film. (C) Bending curvature as a function of light power density, corresponding to the BOPP/LSPR-SNC/PET actuators and the BOPP/PET film. (D) Blocking force as a function of light power density, corresponding to the BOPP/LSPR-SNC/PET actuators and the BOPP/PET film.

a homogeneous coating on the PET surface. After drying, BOPP films (with a thickness of ~40 μm) were attached on top of the LSPR-SNC films, forming the BOPP/LSPR-SNC/PET actuators. Fig. 2B and C are scanning electron microscopy (SEM) images showing the cross-sectional structures of the coated LSPR-SNC layer and the final actuator. As it can be observed, the thickness of the LSPR-SNC layers is about 5 μm.

As shown in Fig. 3A, all the prepared BOPP/LSPR-SNC/PET actuators are colorless and transparent, and even not easy to see by the naked eye. The transmittance spectra shown in Fig. 3C demonstrated that all the actuators exhibit a transmittance higher than 72% at 600 nm, while these actuators possess remarkable absorption in the infrared region, implying prominent photothermal conversion ability. It is required to point out that after being coated on the PET substrate, the LSPR-SNCs no longer exhibit independent resonant absorption peaks. However, they present broader band absorption in the infrared region, which is owing to the intercoupling of plasmon polaritons between individual LSPR-SNCs.[22,23] As shown in Fig. 3B, the actuators can be effectively heated with the NIR light irradiation (200 mW cm^{-2}). Among the three kinds of BOPP/LSPR-SNC/PET actuators, the BOPP/ITO/PET actuator exhibits the most superior photothermal ability, which can be heated up to 54 °C under the NIR light irradiation.

Actuation performances

To study the actuation performances, the prepared BOPP/LSPR-SNC/PET actuators were fixed onto glass slides, respectively, as shown in Fig. 4A. When irradiated by NIR light for 5 s, the LSPR-SNC layers absorb photons and convert them into thermal energy. The temperature of the actuators increases, which induces a remarkable bending of these actuators to the PET side. The bending is attributed to differences in the thermal expansion abilities between PET and BOPP. The coefficient of thermal expansion (CTE) of BOPP is 137 ppm K^{-1},[24] while that of PET is only 59.4 ppm K^{-1}.[25] With the increase of the NIR light power, the temperature and the bending curvature of the actuators increase, as shown in Fig. 4B and C. The calculation of the bending curvature is shown in Fig. S5 and Note S2 of the ESI.† As a comparison, a BOPP/PET bilayer film was also tested under similar NIR light irradiation. It showed only a tiny temperature change and a slight bending, which might be induced by the thermal conduction of the air (Fig. S6 in the ESI†). It can be seen that the BOPP/ITO/PET actuator exhibited the most remarkable photothermal conversion and actuation performance. With the NIR light irradiation of 500 mW cm^{-2}, the temperature change of the BOPP/ITO/PET actuator was up to 43 °C and the curvature reached 0.66 cm^{-1}. It should be pointed out that, such actuation performance has already approached the deformation limitation of BOPP-PET actuation system. Because a higher temperature would damage the used commercial BOPP films. For a clear comparison, we carried out a simulation to calculate the theoretical limitation of our BOPP-BET thermal actuation system. The maximum temperature change was set to be 45 °C. We approximated our actuation system to a bilayer configurational model, as shown in Fig. S7 and Note S3 of the ESI.† The calculated curvatures ($1/\rho$) as a linear function of temperature change are figured out and graphed in Fig. S8 (ESI†). When the temperature

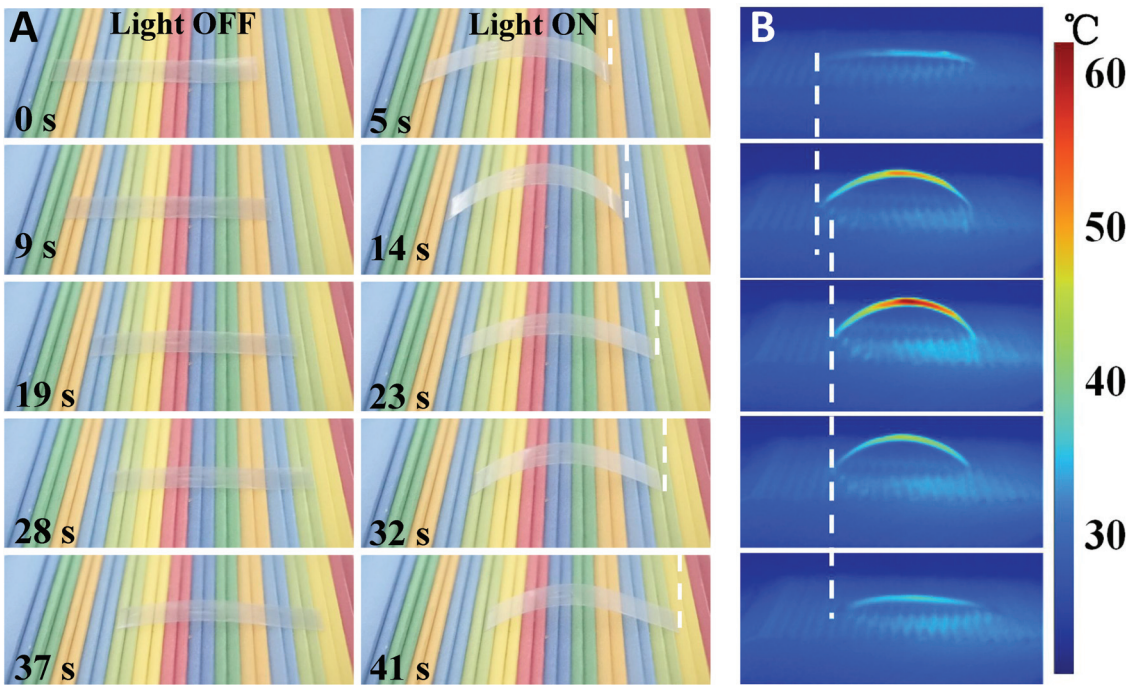

Fig. 5 (A) Photographs displaying the worm-like robot fabricated by BOPP/ITO/PET actuators mimicking a "worm" crawling on a multi-colored ratchet-shaped substrate. (B) Infrared thermal images monitoring the crawling motion of the worm-like robot.

change reaches 45 °C, the calculated curvature is 0.73 cm^{-1}. Obviously, the performance of BOPP/ITO/PET actuator upon light irradiation of 500 mW cm^{-2} is already quite close to this value.

To evaluate the power of these actuators, the blocking forces of these BOPP/LSPR-SNC/PET actuators upon various light irradiation were also measured, and are shown in Fig. 4D. The force density, which is defined as the blocking force divided by the weight of the actuator, is a key factor for the effective force generation of an actuator. When the BOPP/ITO/PET actuator was irradiated by NIR light (500 mW cm^{-2}), the blocking force reached up to 1.35 mN. As the weight of the actuator sample was 20.5 mg, the force density was calculated to be 6.6 for the BOPP/ITO/PET actuator. Finally, the actuation performances of BOPP/LSPR-SNC/PET actuators have no significant degradation under NIR light (500 mW cm^{-2}) irradiation after 100 cycles (Fig. S9, ESI†), indicating good reliability and stability of the actuators.

Applications

To demonstrate the advantages of remote control and invisible manipulation of these actuators, a transparent worm-like robot was fabricated using the BOPP/ITO/PET actuator, as shown in Fig. 5A. To ensure that the light stimulation is indiscernible, an optical filter (>800 nm) was installed on the lamp. For illustrating the camouflage ability of the actuator, a multi-colored ratchet-shaped substrate was used. This biomimic robot was initially straight. When the driving light was turned on, it bent and took a step forward. When the driving light was turned off, it returned to the original straight shape. With the driving light being on and off alternately, such a robot was able to crawl forward on the ratchet-shaped substrate, imitating the motion of a "worm". Each step cost about 10 s. A video recording the motions of the worm-like robot is provided as Movie S1 in the ESI.†

It is worth noting that as the worm-like robot is colorless and transparent, it is almost concealed into the multi-colored background and is not easy to see by the naked eye, demonstrating a passive camouflage strategy. A relatively clear visualization can be obtained only if it bends, owing to the contrast caused by the reflection of the curving surface. Meanwhile, owing to the optical filter, the driving light is in the infrared light region, which is also invisible for the naked eye. The influence of light on the robot can only be detected using an infrared thermal imager (Fig. 5B). It can be seen that when the robot is bending, its temperature increases obviously, indicating the photothermal effect. Hence, the soft robots based on the BOPP/LSPR-SNC/PET actuators are nearly "indiscernible" due to their transparent appearance and can be remotely manipulated through "invisible" signals (infrared light), indicating the potential applications in the fields of camouflage soft robots.

Furthermore, to show the advantages of our transparent actuators in the camouflage soft robots more intuitively, a glasswing butterfly robot was designed. The forewings of the butterfly robot were fabricated using BOPP/ITO/PET actuators,

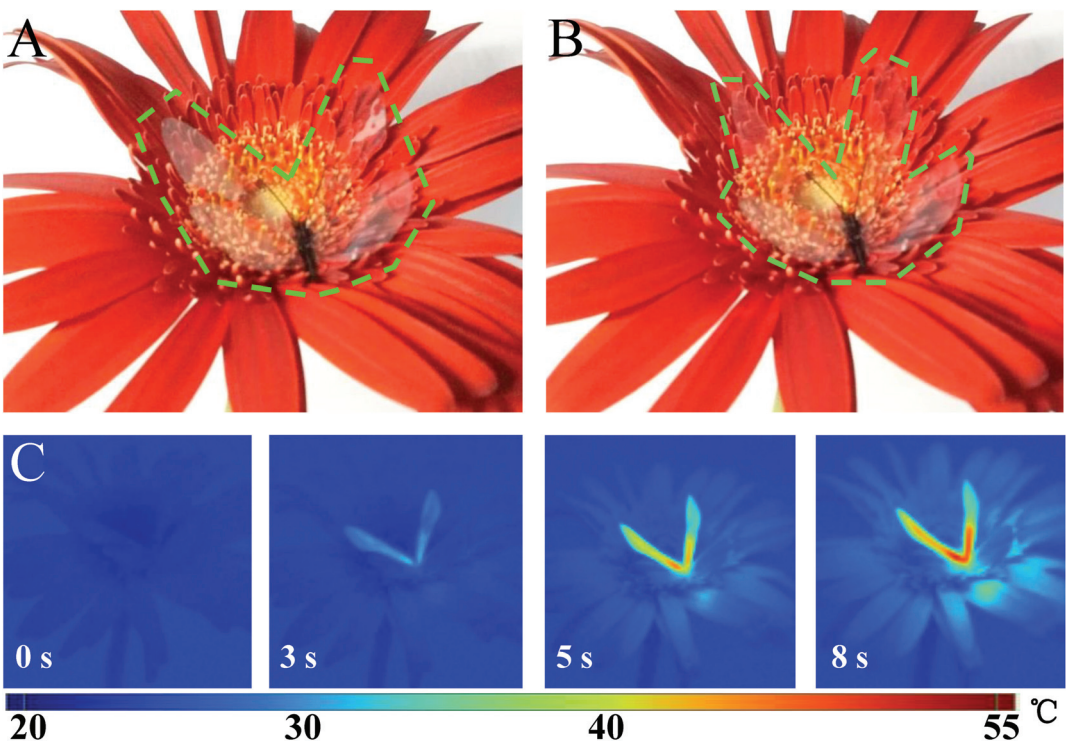

Fig. 6 (A) Photograph of the glasswing butterfly robot on a flower. The dashed lines are used for easy visualization of the transparent robot. (B) Photograph of the glasswing butterfly robot driven by infrared light. (C) Infrared thermal images monitoring the motion of the glasswing butterfly robot.

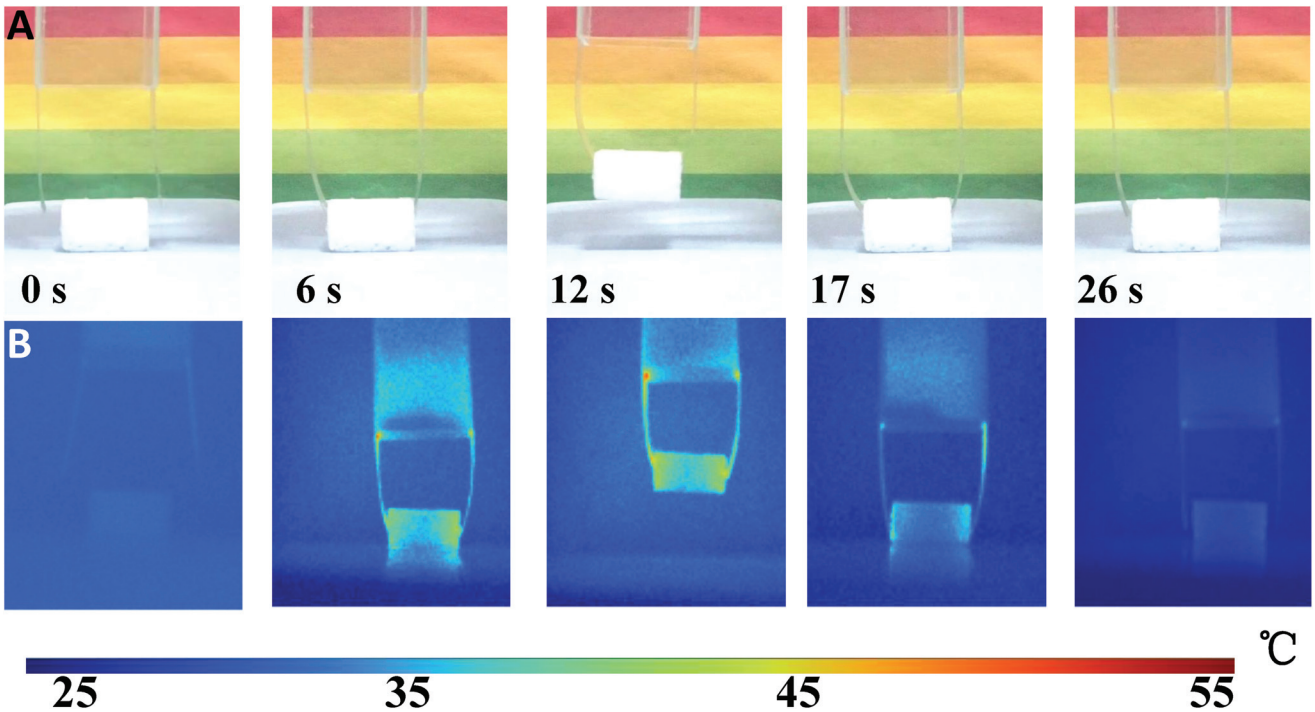

Fig. 7 (A) Photographs captured during the grabbing and releasing motions of the robot hand with two fingers made of BOPP/ITO/PET actuators. (B) Infrared thermal images monitoring the grabbing and releasing motions of the robot hand.

while the hindwings were fabricated using PET films for comparison. This butterfly robot was placed on a flower (Fig. 6A). Owing to the transparent appearance, the butterfly robot almost concealed into the background, showing the camouflage function. When the butterfly robot was irradiated by infrared light, its forewings flapped, while its hindwings remained still (Fig. 6B). The motion of this butterfly robot can be captured through an infrared thermal imager, as shown in Fig. 6C. A video recording the motions of the glasswing butterfly robot driven by infrared light is also provided as Movie S2 in the ESI.†

The last application was a robot hand with two artificial fingers, which were fabricated using the BOPP/ITO/PET actuators. As shown in Fig. 7A, when the infrared light irradiation was on, the two fingers were getting closer and could grab an object within 3 s. Then they could lift up and lay down the object. When the lamp was turned off, the two fingers released the object within 4 s. A video recording the motions of the robot hand is provided as Movie S3 in the ESI.† The influence of infrared light on the robot hand during the operation process is shown in Fig. 7B.

Conclusions

In summary, a series of LSPR-SNCs, including ITO nanoparticles, $W_{18}O_{49}$ nanorods and CuS nanoplates, are synthesized and employed as the photothermal conversion agents in polymer-based photothermal actuators. These actuators are colorless and transparent, exhibiting remarkable deformation under NIR light irradiation. For the demonstration of these advantages, a worm-like robot, a glasswing butterfly robot and a two-finger robot hand were fabricated based on BOPP/LSPR-SNC/PET actuators. Such actuators not only demonstrate the advantages of remote manipulation, but also exhibit superiority of inconspicuousness in both the actuator appearance and the driving signal. Therefore, this work is expected to open a new way for camouflage soft robots and biomimic applications.

Experimental section

Chemical reagents

Indium acetylacetonate ($In(C_5H_7O_2)_3$), acetylacetone tin chloride ($Sn(C_5H_7O_2)_2Cl_2$), tungstic acid (H_2WO_4), copper iodide (CuI), sulfur (S), oleylamine ($C_{18}H_{37}N$), octadecene ($C_{18}H_{36}$), polymethyl methacrylate (PMMA) and methylbenzene (C_7H_8) were purchased from Sinopharm Chemical Reagent Company. The PET films and BOPP films coated with acrylic ester were all commercial products.

Synthesis of the ITO nanocrystals

Typically, 0.9 mmol indium acetylacetonate ($In(C_5H_7O_2)_3$) and 0.1 mmol acetylacetone tin chloride ($Sn(C_5H_7O_2)_2Cl_2$) were dissolved in a mixture solvent of 5 mL oleylamine and 15 mL octadecene. The resulting mixture was heated at 120 °C for 30 min under N_2 flow to get rid of oxygen and water, and then

was heated up to 270 °C, and kept at this temperature for 3 h. After the reaction system was cooled to room temperature, some amount of ethanol was added to precipitate the deep blue product.

Synthesis of the $W_{18}O_{49}$ nanorods

Typically, 1 mmol tungstic acid (H_2WO_4) was dissolved in 15 mL oleylamine. The resulting mixture was heated at 120 °C for 30 min under N_2 flow to get rid of oxygen and water, and then was heated up to 290 °C, and kept at this temperature for 1 h. After the reaction system was cooled to room temperature, some amount of ethanol was added to precipitate the deep blue product.

Synthesis of the CuS nanoplates

Typically, 1 mmol CuI and 2 mmol sulfur were dissolved in 15 mL oleylamine. The resulting mixture was heated at 120 °C for 30 min under N_2 flow to get rid of oxygen and water, and then was heated up to 180 °C, and kept at this temperature for 30 min. After the reaction system was cooled to room temperature, some amount of ethanol was added to precipitate the deep green product.

Fabrication of the LSPR-SNC oily inks

Typically, the prepared LSPR-SNCs (0.05 mg) were dispersed in 5 mL methylbenzene, and then 0.025 mg of PMMA was added as the bonding agent. After stirring for about 15 min, a homogeneous colloidal ink was obtained. The color was dark blue for $W_{18}O_{49}$ LSPR-SNC-based ink, while that for the CuS and ITO ones was dark green.

Fabrication of the photothermal actuators

PET films (with a thickness of 25 μm) were cut into strips (5 mm × 40 mm). The LSPR-SNC oily ink was coated on the PET strips by drop-casting, forming a photothermal conversion layer. After being dried for 30 min, a BOPP film was pasted on top of the photothermal conversion layer to form the BOPP/LSPR-SNC/PET actuators.

Fabrication of the worm-like crawling robot

A PET film (with a thickness of 25 μm) was cut into a strip (10 mm × 60 mm). The ITO oily ink was coated on the PET film by drop-casting, forming a photothermal conversion layer. After being dried for 30 min, a BOPP film was pasted on top of the photothermal conversion layer to form the BOPP/ITO/PET actuator, which was also the worm-like crawling robot. After that, the worm-like crawling robot was placed on a multi-colored ratchet-shaped substrate, which was made of glass slides wrapped by colourful papers, as shown in Fig. S10 (ESI†).

Fabrication of the glasswing butterfly robot

PET films (with a thickness of 25 μm) were cut into strips with dimensions of 20 mm × 30 mm. The ITO oily ink was coated on the PET films by drop-casting, forming a photothermal conversion layer. After being dried for 30 min, BOPP films were pasted on top of the photothermal conversion layer to form the BOPP/ITO/PET actuators. After that, two BOPP/ITO/PET actuators were cut as forewings with dimensions of 25 mm × 13 mm. Two PET films were cut as hindwings with dimensions of 16 mm × 13 mm. A strip PET film (18 mm × 2.5 mm) was painted black with a marker pen and used as the body part of the glasswing butterfly robot. The structure of the glasswing butterfly robot is shown in Fig. S11 (ESI†).

Fabrication of the two-finger robot hand

PET films (with a thickness of 25 μm) were cut into strips (10 mm × 50 mm). The ITO oily ink was coated on the PET films by drop-casting, forming a photothermal conversion layer. After being dried for 30 min, BOPP films were pasted on top of the photothermal conversion layer to form the BOPP/ITO/PET actuators, which were used as the artificial fingers of the robot. After that, two BOPP/ITO/PET actuators were attached to a transparent hollow glass cuboid (18 mm × 18 mm × 70 mm) to form the two-finger robot hand.

Characterization

The TEM images were taken using a field emission TEM (FEI Tecnai G2 F20). The SEM images were captured using a field-emission SEM (Hitachi SU8010). The absorption spectra of the nanocrystal colloids and the transmittance spectra of the prepared actuators were recorded using a UV-vis-IR spectrophotometer (Lambda 900). Bending angles of the actuators were obtained by reading from optical images and videos, which were captured using a digital camera (SONY ILCE 6000). The bending curvatures were further calculated from the bending angle and length of the actuator (detailed calculation principle is shown in Note S2 of the ESI†). A NIR light source (Philips BR125) was used for light-driven actuation. The light power density was measured using an IR power meter (Linshang LS122A). The temperature was recorded using a laser sight infrared thermometer (Optris LS) with a temperature resolution of 0.1 °C. The temperature data were obtained from the BOPP surface of the actuator. An infrared thermal imager (Fluke Ti10) was used to capture the infrared thermal images of the samples. When we measured the blocking force, an actuator (10 mm × 55 mm) was connected to a PDMS cube (996 mg) as a preload. They were then placed on a precision balance with vertical configurations. The generated forces of the actuator were measured as a function of the NIR light power densities (operating for 10 s).

Conflicts of interest

There are no conflicts of interest to declare.

Acknowledgements

We acknowledge the funding from the National Natural Science Foundation of China (Grant No. 51773039 and

11574312), the Natural Science Foundation of Fujian Province for Distinguished Young Scientists (Grant No. 2017J06014 and 2018J06001), the Education Department of Fujian Province (Grant No. JZ160428), the Fujian Provincial Orienting Sci & Tech Project (Grant No. 2018H0012) and the Open Research Fund Program of the State Key Laboratory of Low-Dimensional Quantum Physics (Grant No. KF201810).

Notes and references

1 V. R. Binetti, J. D. Schiffman, O. D. Leaffer, J. E. Spanier and C. L. Schauer, *Integr. Biol.*, 2009, **1**, 324–329.
2 P. C. Li, Y. Z. Wang, U. Gupta, J. Liu, L. Zhang, D. H. Du, C. C. Foo, J. Y. Ouyang and J. Zhu, *Adv. Funct. Mater.*, 2019, **29**, 1901908.
3 H. Yuk, S. Lin, C. Ma, M. Takaffoli, N. X. Fang and X. Zhao, *Nat. Commun.*, 2017, **8**, 14230.
4 C. Christianson, N. N. Goldberg, D. D. Deheyn, S. Cai and M. T. Tolley, *Sci. Robot.*, 2018, **3**, eaat1893.
5 T. Hwang, H. Y. Kwon, J. S. Oh, J. P. Hong, S. C. Hong, Y. Lee, H. R. Choi, K. J. Kim, M. H. Bhuiya and J. D. Nam, *Appl. Phys. Lett.*, 2013, **103**, 151101.
6 S. E. Zhu, R. Shabani, J. Rho, Y. Kim, B. H. Hong, J. H. Ahn and H. J. Cho, *Nano Lett.*, 2011, **11**, 977–981.
7 U. Kim, J. Kang, C. Lee, H. Y. Kwon, S. Hwang, H. Moon, J. C. Koo, J. D. Nam, B. H. Hong, J. B. Choi and H. R. Choi, *Nanotechnology*, 2013, **24**, 145501.
8 L. Chen, M. Weng, W. Zhang, Z. Zhou, Y. Zhou, D. Xia, J. Li, Z. Huang, C. Liu and S. Fan, *Nanoscale*, 2016, **8**, 6877–6883.
9 H. Kim, H. Lee, I. Ha, J. Jung, P. Won, H. Cho, J. Yeo, S. Hong, S. Han and J. Kwon, *Adv. Funct. Mater.*, 2018, **28**, 1801847.
10 Y. Hu, Z. Li, T. Lan and W. Chen, *Adv. Mater.*, 2016, **28**, 10548–10556.
11 B. Han, Y. Zhang, Q. Chen and H. Sun, *Adv. Funct. Mater.*, 2018, **28**, 1802235.
12 F. Ge, X. Lu, J. Xiang, X. Tong and Y. Zhao, *Angew. Chem., Int. Ed.*, 2017, **56**, 6126–6130.
13 F. Ge, R. Yang, X. Tong, F. Camerel and Y. Zhao, *Angew. Chem., Int. Ed.*, 2018, **57**, 11758–11763.
14 G. Garcia, R. Buonsanti, E. L. Runnerstrom, R. J. Mendelsberg, A. Llordes, A. Anders, T. J. Richardson and D. J. Milliron, *Nano Lett.*, 2011, **11**, 4415–4420.
15 K. Manthiram and A. P. Alivisatos, *J. Am. Chem. Soc.*, 2012, **134**, 3995–3998.
16 G. V. Naik, J. Kim and A. Boltasseva, *Opt. Mater. Express*, 2011, **1**, 1090–1099.
17 J. M. Luther, P. K. Jain, T. Ewers and A. P. Alivisatos, *Nat. Mater.*, 2011, **10**, 361–366.
18 X. Liu, X. Wang, B. Zhou, W. Law, A. N. Cartwright and M. T. Swihart, *Adv. Funct. Mater.*, 2012, **23**, 1256–1264.
19 K. Manthiram and A. Alivisatos, *J. Am. Chem. Soc.*, 2012, **134**, 3995–3998.
20 D. X. Zhu, A. W. Tang, L. Peng, Z. Y. Liu, C. H. Yang and F. Teng, *J. Mater. Chem. C*, 2016, **4**, 4880–4888.
21 G. V. Naik, V. M. Shalaev and A. Boltasseva, *Adv. Mater.*, 2013, **25**, 3264–3294.
22 Z. Yin, H. Li, W. Xu, S. Cui, D. Zhou, X. Chen, Y. Zhu, G. Qin and H. Song, *Adv. Mater.*, 2016, **28**, 2518–2525.
23 Z. Yin, D. Zhou, W. Xu, S. Cui, X. Chen, H. Wang, S. Xu and H. Song, *ACS Appl. Mater. Interfaces*, 2016, **8**, 11667–11674.
24 M. Weng, P. Zhou, L. Chen, L. Zhang, W. Zhang, Z. Huang, C. Liu and S. Fan, *Adv. Funct. Mater.*, 2016, **26**, 7244–7253.
25 Y. M. Lee, O. J. Kim, D. K. Choi and J. Yu, *Macromol. Res.*, 2016, **24**, 1062–1069.